Applied Surface Science 667 (2024) 160345

Contents lists available at ScienceDirect

Applied Surface Science

journal homepage: www.elsevier.com/locate/apsusc

Full length article

Sodium Carbonate ion complexes modify water structure at electrode interfaces

Amro Dodin [a,1], Gang-Hua Deng [b,1], Jaclyn A. Rebstock [c], Quansong Zhu [c], David T. Limmer [a,d,e,f,*], L. Robert Baker [c,*]

[a] Chemical Sciences Division, Lawrence Berkeley National Laboratory, Berkeley 94720, CA, USA
[b] State Key Laboratory of Information Photonic and Optical Communications and School of Science, Beijing University of Posts and Telecommunications (BUPT), Beijing 100876, PR China
[c] Department of Chemistry, The Ohio State University, Columbus, OH 43210, USA
[d] Department of Chemistry, University of California Berkeley, Berkeley 94720, CA, USA
[e] Material Sciences Division, Lawrence Berkeley National Laboratory, Berkeley 94720, CA, USA
[f] Kavli Energy NanoSciences Institute, University of California, Berkeley 94720, CA, USA

ARTICLE INFO

Keywords:
CO_2 reduction
Sum frequency generation spectroscopy
Electrochemistry
Ion pair
Interfacial water structure

ABSTRACT

Water structure near electrode interfaces may play an important role in controlling CO_2 electroreduction. Using plasmon-enhanced vibrational sum frequency generation spectroscopy, we demonstrate the emergence of an interfacial water subpopulation with large electric fields along their OH bonds, when Na_2CO_3 ions are present near the electrode under applied potential. With molecular dynamics simulations, we show that the approach of aqueous Na_2CO_3 to electrodes is coupled to the formation of structured and oriented ion complexes, and that the emergent water population is associated with the first solvation shell of these complexes. This water subpopulation is seen even when the sole source of CO_3^{2-} is its *in-situ* generation from CO_2, indicating that the interfacial species investigated here are likely ubiquitous in CO_2 electroreduction contexts.

1. Introduction

Electrochemical CO_2 reduction (CO_2R) offers the promise of converting CO_2 into renewable fuels or value-added chemical feed stocks [1–3]. However, controlling the efficiency and selectivity of CO_2R remains a significant challenge. While much effort has been devoted to catalyst design, it is also widely reported that the electrolyte composition has a significant effect on reaction kinetics [4–10]. In electrocatalytic processes, the electrode and the electrolyte represent the two sides of the solid–liquid interface, which forms the local environment for the electron and proton transfer reactions that drive catalysis. The interplay of these two materials, creates a unique interfacial environment where electrode polarization can modulate local electrolyte composition, ion pairing, and the resulting interfacial solvation structure, in turn influencing the electrochemical kinetics that control the viability of critical processes such as CO_2 conversion. Here we use vibrational spectroscopy and molecular simulation to study the electrode–electrolyte interface under conditions relevant to CO_2R. We reveal how ions like Na^+ and CO_3^{2-}, that are prevalent in CO_2 systems, can form correlated ion complexes that modulate electric fields at the interface through their polarization of the surrounding water.

Many reports indicate that the identity of the hydrated cation at the charged interface determines its catalytic activity, although the mechanism behind specific ion effects on CO_2R remains an open question. Early explanations explored the structure of the double layer and the corresponding potential drop across the interface [11,12], while more recent studies have shown that interfacial solvation structure can mediate reactions [10,13,14], arguing for explicit treatment of solvation in kinetic models of CO_2R [15,16]. While it is known that the presence of cations at the charged interface is integral for CO_2R activity [17], the mechanism behind cation-dependent efficiency trends are still widely debated. Possible molecular reasons for the relation between cation identity and efficiency include cation-dependent pKa of hydrolysis [18], cation-specific electric field effects [19], and the effect of specific cations on the solvation-induced Onsager reaction field present at the interface during CO_2R [10]. All of these theories point to the need for a molecular understanding of ion interactions at electrified surfaces and the effect of discrete ions and ion pairs on the alignment and hydrogen-bonding structure of interfacial water.

It is reported that the presence of ion pairs can significantly impact the kinetics of electrochemical reactions [20]. While ion pairing in

* Corresponding authors.
E-mail addresses: dlimmer@berkeley.edu (D.T. Limmer), baker.2364@osu.edu (L.R. Baker).
[1] Contributed equally to this work.

https://doi.org/10.1016/j.apsusc.2024.160345
Received 23 January 2024; Received in revised form 10 May 2024; Accepted 19 May 2024
Available online 27 May 2024

concentrated aqueous solutions is widely reported [21,22], comparatively less is known about ion pairing and ion solvation at electrified interfaces, although there is some theoretical evidence that suggests ion pairing is enhanced near an aqueous electrode interface [23]. Solvent separated ion pairs of alkali halides were observed at negative applied potentials on a silver electrode using surface-enhanced Raman spectroscopy (SERS) [24]. In that study, the observed SERS spectra of water were shown to depend both on the cation composition and the applied potential, which was explained by the gradual desolvation of cations at negative surface potentials leading to the interfacial accumulation of solvent-separated ion pairs. Zou et al. studied the structure of water on silver electrodes in alkali sulfate and perchlorate solutions [25]. They found that the effect of the anion on the Raman spectra of water is significant, even at negative potentials. This result is somewhat counterintuitive since anions would be repelled from negatively charged surfaces; however, this was attributed to the formation of ion pairs at the interface.

Ion pair formation in concentrated aqueous solutions can alter the prediction of theories developed for dilute electrolyte solutions [26,27] by modifying osmotic and activity coefficients [28], reducing electronic conductivity [29], and changing the structure of the double layer near charged electrodes [30,31]. This phenomenology becomes more complex near aqueous interfaces, where ion-interface interactions and modified solvent statistics couple the pairing of ions and their approach to the interface [32,33]. In particular, a recent series of studies suggests that the reverse fractionation of Na_2CO_3 at the air–water interface, where carbonate ions become more surface active, may arise due to the association of ions into agglomerates near the interface [34,35].

Understanding the specific effects of carbonate on interfacial solvation structure and its participation in ion pairing is of particular interest because carbonate is ubiquitous in CO_2-saturated aqueous solutions suggesting that it likely plays a role in templating the interfacial solvation during CO_2R. Compared to simple anions such as halides and anions with higher symmetry (sulfate, perchlorate), carbonate has a planar structure, which could have non-intuitive consequences on the alignment of interfacial water. Due to the divalent, polarizable nature of carbonate, its physical interactions at the electrode–electrolyte interface are not trivial to predict. All these factors motivate the present study, which seeks to provide a molecular understanding of the underlying physics, which govern ion interactions and solvation at electrode surfaces in the presence of carbonate.

In this study, we employ vibrational sum frequency generation spectroscopy (VSFG) to probe the alignment of interfacial water in carbonate-containing electrolyte solutions at a gold electrode under applied potentials relevant for CO_2R. We observe potential-dependent differences in the interfacial water spectrum, which are strongly influenced by the presence or absence of the carbonate anion as well as the electrolyte cation. With the aid of molecular dynamics simulations, these spectral differences are correlated with the effect of carbonate on the potential-dependent alignment of interfacial water and the formation of a sodium-carbonate ion complex, which is over-represented near the interface and significantly influences the spectral region of interest.

2. Methods

2.1. Experimental

The specifics of the VSFG system have been discussed in previous work [10,14,36–38]. Briefly, a Ti: sapphire regenerative amplifier (Spectra Physics-Solstice) with 90 fs pulse duration (2 kHz, 7 W) at 800 nm functions as the pump laser. An optical parametric amplifier (TOPAS Prime) is powered by 70% of this output, which then generates the signal and idler to a noncollinear difference frequency generation (DFG) stage. The remaining 30% is spectrally narrowed to about 10 cm^{-1} using an air-gap etalon (TecOptics). The beams hit the sample at a 56° angle, following the Kretschmann method. The IR beam, centered around 3450 cm^{-1} in the OH stretch region, has an energy of 3 μJ, while the 800 nm picosecond beam has an energy of roughly 10 μJ. For the water spectra measurements, a potential step ranging from −0.1 to −1.0 V against Ag/AgCl was applied to the Au electrode. Each spectrum was gathered by delaying the visible beam relative to the IR beam by approximately 466 fs, with a 2-minute integration time. Further information about the VSFG electrochemical cell can be found in our previous work. This VSFG electrochemical cell uses a backside configuration with plasmonic enhancement, enabling *in-situ* observations of the Au-electrolyte interface at current densities surpassing 1 mA/cm^2, without the presence of mass transport limitations. A typical cyclic voltammetry of Na_2CO_3 (0.05M) purged with CO_2 with the spectro-electrochemical cell can be found in Supporting Information Figure S1.

The Au electrodes for VSFG studies were prepared by depositing 35 nm of Au onto CaF_2 windows by electron beam evaporation (Denton DV-502A E-Gun Evaporator). Before Au was deposited, the CaF_2 windows were cleaned using basic Piranha solution (5:1:1 $H_2O/H_2O_2/NH_4OH$) at 80 °C for an hour. The BioLogic SP-50 potentiostat was employed for electrochemical measurements. The electrochemical cell was made up of a Au working electrode, a leakless Ag/AgCl reference electrode (eDAQ ET072-1), and a Pt mesh counter electrode, with a Nafion membrane separating the cathode and anode compartments. The electrolytes were prepared by purging 0.1 M $NaHCO_3$, 0.1 M $CsHCO_3$, 0.1 M NaCl (99.99%) and 0.05 M Na_2SO_4 (99.99%) with either Ar or CO_2 (Praxair, 99.999%) for 20 min.

2.2. Molecular dynamics simulation

To gain microscopic insight into the structure of the three ion Na_2CO_3 complex, its spatial arrangement relative to the interface, and the vibrational spectrum of its solvation shell, we performed a series of MD simulations using the LAMMPS software package [39]. We considered dilute aqueous solutions of Na_2CO_3 in the bulk as well as near an electrode. We studied the ions near an electrode at its potential of zero charge as well the anode and cathode of a cell under a 1 V potential drop. Free energy surfaces (FES) for the ion complex were constructed in each chemical environment using a two dimensional umbrella sampling scheme over the distances between the center of mass of the carbonate anion, and each Na^+ cation denoted r_1 and r_2 [40,41]. A set of 14 harmonic biases, $U_{\text{bias}}(r_1, r_2) = k_1(r_1 - r_1^{(\text{eq})})^2 + k_2(r_2 - r_2^{(\text{eq})})^2$, was used for each distance coordinate, with minima $r_{1,2}^{(\text{eq})}$, spaced by 0.5 Å between 2.5 Å and 9.0 Å for a grid of 196 bias windows, with a spring constant of $k_1 = k_2 = 10$ kCal/mol/Å^2. In addition, a set of 21 harmonic biases were used with respect to the anion distance from the electrode, z_a, while also holding the ion-complex in a contact configuration $U_{\text{bias}}(r_1, r_2) = k_1(r_1 - r_1^{(\text{eq})})^2 + k_2(r_2 - r_2^{(\text{eq})})^2 + k_z(z_a - z_a^{(\text{eq})})^2$, with $k_1 = k_2 = k_z = 10$ kCal/mol/Å^2, $r_i^{(\text{eq})} = 2.5$ Å, and $z_a^{(\text{eq})}$ spaced by 0.5 Å from van der Waal's contact $z_a = 0$ Å to 10 Å. Each bias window was sampled for at least 1 ns, recording ion configurations every 0.25 ps and water configurations every 1 ps. The Weighted Histogram Analysis Method (WHAM) was then used to construct an unbiased FES from biased simulations [42–45], and to compute unbiased histograms and averages [44]. In the electrode simulations, CO_3^{2-} was also held at the interface by a harmonic bias with a 10 kCal/mol/Å^2 in order to probe the interfacial double layer.

Each bulk water simulation contains 234 water molecules, 1 CO_3^{2-} anion and 2 Na^+ cations in a fully periodic $\sim 18 \times 18 \times 18$ Å liquid region, consistent with a dilute 2.6 mM solution. Electrode simulations, instead contained 468 water molecules in a $\sim 18 \times 18 \times 36$ Å liquid region (periodic in x and y), with two atomistic electrodes consisting of 3 layers of Au atoms in an FCC structure with a lattice constant of $a_{\text{Au}} = 4.07$ Å truncated to reveal the (100) surface. The electrode interfaces were taken parallel to the xy plane with normal vectors in the $\pm z$ directions. The electrode simulations are large enough to

include a bulk-like region between the interfacial regions with a Debye length of ~8 Å. The electrodes were treated as ideal conductors [46–48] as implemented in the LAMMPS ELECTRODE package [49]. All non-hydrogen electrolyte atoms were modeled with Drude oscillator polarizable forcefield [50,51] using the LAMMPS DRUDE package [52] to provide an accurate treatment of the forces on the highly polarizable carbonate anion [53–55]. Symmetrized Drude force fields were used to improve numerical stability with a Drude mass of $m_D = 0.8$ g/mol [56]. The system was propagated using a dual Nosé–Hoover thermostat [50,57] using Nosé–Hoover chains [58,59] at 300 K for the atoms and 1 K for the fictitious Drude sites with a relaxation time of 0.01 fs^{-1} and a timestep of 1 fs. The water was treated using the swm4-ndp model [60], and the ions used a polarizable force field previously used to study the air–water interface [55]. The water molecules and carbonate anion were propagated as rigid bodies using the symplectic rigid-body integrator of Kamberaj et al. [61] freezing all internal coordinates at their equilibrium values.

The vibrational spectra of water's OH bond stretch, relevant to the spectral region of interest, was computed using the field mapping method [62–66]. In this approach, the electric field is evaluated at each hydrogen atom and is computed and projected along the bond. The frequency of the OH bond stretch, ω, then undergoes a vibrational Stark shift from its vacuum value, ω_0, due to this projected electric field, ε. In liquid water, this vibrational Stark shift can be fit to experimental Raman spectra or to electronic structure calculations and is well approximated by a linear fit of the form

$$\omega = \omega_0 + \Delta\varepsilon, \tag{1}$$

where $\omega_0 = 3670$ cm^{-1} and $\Delta = 160.5$ $cm^{-1}/(V/Å)$. Using this expression, the vibrational spectra of water is constructed as histograms of the field along OH bonds. This approach assumes that each OH bond behaves as an independent oscillator, neglecting vibrational coupling between OH bonds, an assumption that is nearly exact for dilute HOD in D_2O but an approximation for pure H_2O. It also assumed that the spectra is purely inhomogeneously broadened. Nevertheless, it has been successfully employed to study multiple forms of vibrational spectroscopy in water [67–70].

3. Results and discussion

3.1. Vibrational sum frequency generation spectroscopy

VSFG, a surface-specific technique, is widely utilized for studying molecular orientation, dynamics, and chemical reactions on surfaces [71–75]. The instrument, including the VSFG electrochemical cell, enables *in-situ* measurements of the Au-electrolyte interface at high current densities without mass transport limitations. By employing this instrument, the spectra of interfacial water at the Au-electrolyte interface were measured. The VSFG spectra of interfacial water in 0.05 M Na_2CO_3 and Cs_2CO_3 saturated with CO_2, plotted as a function of applied potential, are shown in Fig. 1. Interference of the non-resonant signal from the electrode and electrolyte contribution could result in complicated intensity spectra, so before any further discussion, we would like to point out that as shown in Figure S2-S5, the non-resonant signal is negligible in our spectra and does not contribute to the main features in the spectra. The line shape of the VSFG spectra could be distorted by the dispersion of the Fresnel factors at the interface. Bonn and coworkers showed that the dispersion of the Fresnel factors at a prism-gold-water interface is as large as it dominates the spectral shape [76]. To eliminate the Fresnel factor effect on the spectra, the Fresnel factors are calculated and shown in Figure S6a. As shown in Figure S6b and S6c, there are no significant differences between the Fresnel factor corrected and uncorrected spectra. However, all the spectra in Figure 1–3 are all Fresnel factor corrected.

As demonstrated in several previous studies, the $\chi^{(3)}$ bulk contribution in interfacial water spectra is common at charged interfaces [77–82]. In cases where $\chi^{(3)}$ dominates the signal, the surface sensitivity of SFG is compromised, and the spectrum reflects bulk rather than interfacial properties. Due to the scaling of $\chi^{(3)}$ with the magnitude of a DC field, this consideration becomes even more important when the interfacial electric field is large as is often the case for electrochemical interfaces. Before further analysis, it is therefore important to consider the possible effect of $\chi^{(3)}$ on the experimental spectra reported here. To consider this question, we first note that at high electrolyte concentrations the Debeye length becomes small, and $\chi^{(3)}$ contributions are suppressed. Previous work has shown that $\chi^{(3)}$ contributions become negligible at concentrations above 0.01 M [83]. Here we employ an electrolyte concentration of 0.1 M corresponding to a Debeye length of less than 1 nm, indicating that SFG signal from bulk water will be largely suppressed. Second, it has been shown by Eftekhari-Bafrooei et al. that the T_1 vibrational relaxation time of interfacial water is significantly longer than bulk water due to decreased rate of vibrational energy transfer at an interface [83]. Because the coherent dephasing time (T_2^*) is influenced by the rate of vibrational energy transfer, this will result in faster dephasing of bulk water relative to the surface. Introducing a time delay of the 800 nm beam relative to the broadband IR will selectively suppress the $\chi^{(3)}$ contribution, although the degree of suppression will depend on the relative dephasing times of bulk and interfacial water. It is common to estimate the dephasing lifetime from linewidth measurements. The FWHM of the 3400 cm^{-1} peak measured here is 65 cm^{-1} (see Table S1), compared to 150 cm^{-1} in bulk water [78]. Considering a 467 fs time delay between IR and 800 nm pulses and assuming homogeneous broadening, $\chi^{(3)}$ would be nearly entirely suppressed. However, in practice inhomogeneous broadening is significant making the exact degree of $\chi^{(3)}$ suppression difficult to determine, and this will require future measurements based on phase-sensitive, heterodyne detection.

To assess the extent to which the combination of short Debeye length and fast dephasing of bulk water effectively suppress the $\chi^{(3)}$ contribution in the present spectra, we note that there is no evidence of any interference between $\chi^{(3)}$ of bulk water and the free-OH peak. This is indicated by the free-OH peak position, which does not shift as a function of applied potential (see Fig. 1). In contrast, Ohno et al. have shown that in cases where $\chi^{(3)}$ is significant, the position of the free-OH peak shifts significantly with applied potential due to phase interference with the $\chi^{(3)}$ contribution of bulk water [77]. The absence of these phase effects in the free-OH region provide evidence that bulk contributions from $\chi^{(3)}$ are small. Even more importantly, the bulk water peak at 3200 cm^{-1} is notably absent from the measured spectra. If $\chi^{(3)}$ were contributing, this characteristic peak from bulk water would be prominent. Based on these observations, we conclude that $\chi^{(3)}$ contributions from bulk water have only a minor effect on the spectra reported here. Although the $\chi^{(3)}$ bulk contribution in the current work is small, disentangling the $\chi^{(3)}$ bulk contribution remains an important consideration to gain a detailed physical picture of the interfacial solvation structure. To achieve this phase-sensitive SFG/SHG measurements based on heterodyne detection can provide a quantitative analysis of $\chi^{(3)}$ contributions [84–86], and these measurements will be critical to further evaluate the molecular structure of water and ion complexes at electrified interfaces.

When the potential is more positive than −0.7 V vs Ag/AgCl, Na_2CO_3 and Cs_2CO_3 exhibit quite similar features, and two peaks are observed: one sharp peak at around 3725 cm^{-1} and a broad peak at around 3650 cm^{-1}. The broad peak around 3650 cm^{-1} is deduced from fitting of the spectra. The fitting curves of the spectra in Fig. 1 can be found in Figure S7, and the fitting parameters are listed in Table S1 and S2 in the Supporting Information. The sharp peak corresponds to non-hydrogen bonded H_2O molecules, specifically free OH. Previous studies have reported the detection of free OH stretch of interfacial water at the aqueous dielectric interface using VSFG. However, it has only recently been observed at the Au-electrolyte interface under applied potential [87]. This feature indicates the presence of interfacial water

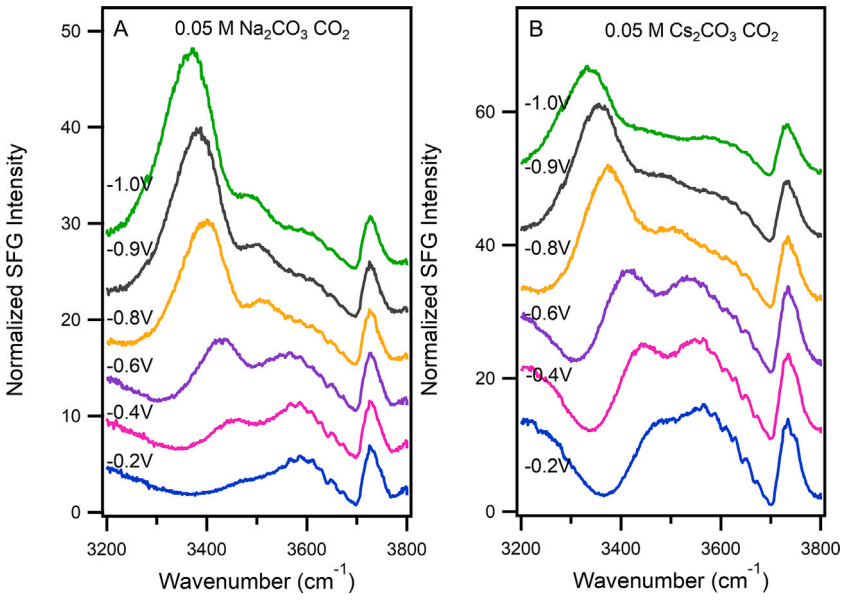

Fig. 1. VSFG spectra of (A) Na_2CO_3 (0.05 M) and (B) Cs_2CO_3 (0.05 M) purged with CO_2 as a function of potential vs Ag/AgCl.

with one non-hydrogen-bonded OH group directed towards the Au electrode, supporting the hydrophobic nature of the Au surface as observed in previous work by Tong et al. [87] The broad peak around 3650 cm^{-1} can be assigned to weakly hydrogen-bonded or singly hydrogen-bonded water. The absence of the peak around 3200 cm^{-1}, which corresponds to strongly hydrogen bonded water [88], in the spectra presented in Fig. 1 suggests that the water structure at the gold electrode surface is relatively disordered as suggested by Nihonyanagi et al. [89]

When a more negative potential is applied, a new peak around 3,400 cm^{-1} becomes evident for both electrolytes. However, the peak is much more prominent for Na_2CO_3 than Cs_2CO_3. This peak might be associated with either liquid-like water or a hydrogen-bonded water network with a coordination lower than the tetrahedral water found around 3200 cm^{-1}. In our previous study, this peak was attributed to Na^+ and CO_3^{2-} ion pair or ion association [38]. To determine the origin of this feature, we investigated the influence of different electrolyte compositions on the water structure at the interface. NaCl and Na_2SO_4 were chosen to compare with Na_2CO_3. As shown in Fig. 2, the peak is not very pronounced in Ar-purged NaCl and is almost absent in Ar-purged Na_2SO_4 solutions, but is more evident in Ar-purged Na_2CO_3 electrolyte. This observation confirms that the feature around 3,400 cm^{-1} is enhanced when carbonate is present at the interface. Given these observations, we attribute the feature to the effect of a carbonate species present in the electrochemical double layer on the water structure. We notice that this peak appears at relatively negative potentials. It might be counterintuitive that anions can influence the water orientation at a negatively charged electrode surface. However, despite their negative charge, anions can be attracted to a Au surface even when a negative potential is applied because of their ion pairing interactions with cations, or because of specific molecular driving forces [90]. In a previous study by Zou et al. it was discovered that the effect of the anion on the Raman spectra of water is significant, even at very negative potentials. They attributed this to the formation of ion pairs at the electrochemical interface [91]. The combination of Figs. 1 and 2 suggest that the presence of both Na^+ and CO_3^{2-} is needed to enhance the intensity of the 3400 cm^{-1} feature, providing indirect evidence for ion pairing interactions. At catalytic potentials, the pH at the interface can get quite high (pH: 9–11, depending on different literature) [92–96]. Most of the HCO_3^- is converted to CO_3^{2-}. As we discussed in our previous work, HCO_3^- may have a minor contribution to the peak around 3400 cm^{-1} [38]. The contribution of OH^- to the peak around 3400 cm^{-1} is not significant as shown in Figure S8. The intensity of the peak around 3350 cm^{-1} is much smaller than the intensity of free OH in 0.1 M NaOH. Additionally, the concentration of OH^- in CO_2-saturated Na_2CO_3 at catalytic potential is expected to be much less than 0.1 M. Therefore, the contribution of OH^- to the peak around 3400 cm^{-1} is not significant.

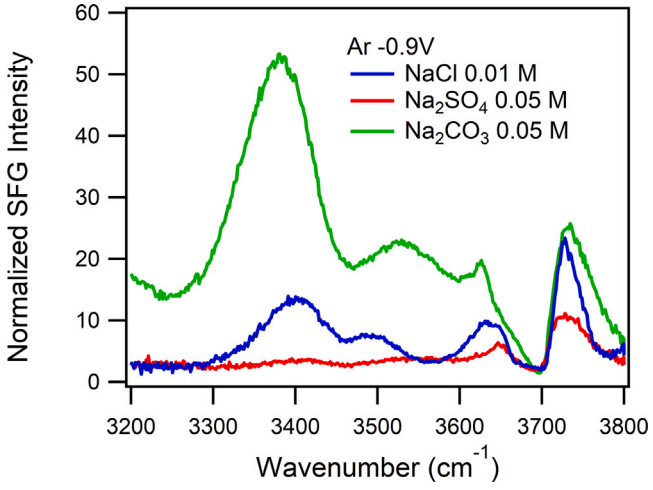

Fig. 2. VSFG spectra of NaCl (0.1 M), Na_2SO_4 (0.05 M) and Na_2CO_3 (0.05 M) purged with Ar at a potential of −0.9 V vs Ag/AgCl.

The carbonate related feature around 3400 cm^{-1} also becomes more prominent in CO_2-purged NaCl electrolyte at catalytic potentials compared to Ar-purged NaCl electrolyte as shown in Fig. 3. Fig. 3(A) shows the potential-dependent water spectra of Ar-purged 0.1 M NaCl electrolyte. Even at −1 V, the peak intensity around 3400 cm^{-1} is quite small; however, when the electrolyte was saturated with CO_2, the peak intensity increased significantly. In CO_2-purged NaCl electrolyte, once the onset of catalytic Faradaic current is reached, the interfacial pH may increase, and CO_3^{2-} anions are generated at the surface resulting in the appearance of the characteristic 3400 cm^{-1} feature. This suggests that the interfacial species responsible for this feature are likely ubiquitous at electrode–electrolyte interfaces during CO_2R electrocatalysis.

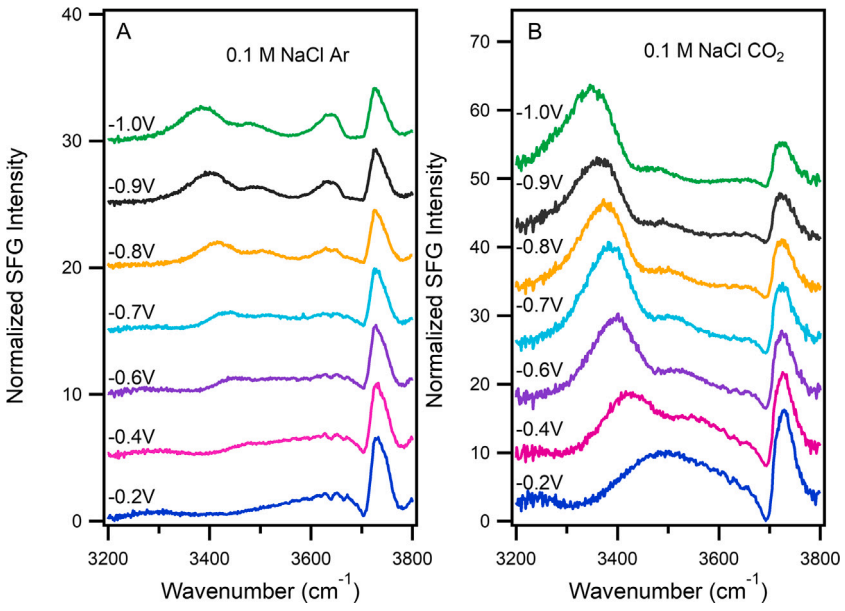

Fig. 3. VSFG spectra of NaCl (0.1 M) purged with Ar (A) and purged with CO_2 (B) as a function of potential vs Ag/AgCl.

3.2. Molecular dynamics simulations

Taken together, the VSFG results show that a unique sub-population of interfacial water emerges or breaks inversion symmetry when both Na^+ and CO_3^{2-} are present near the cathode. This suggests the formation of interfacial ion-complexes with a unique solvation environment, since the spectral peak emerges most strongly in the presence of both ions. The formation of ion-paired complexes is plausible under the concentrations we consider with typical ion–ion separations on the order of the Na^+-CO_3^{2-} Bjerrum length [26], $\lambda_B = 14$ Å, in water. We consider the results of MD simulations to gain microscopic insight into (1) the thermodynamics of forming Na^+-CO_3^{2-} ion-complexes and how this may change near the interface, (2) the structure of these complexes and their orientation relative to the interface, and (3) the vibrational spectrum and orientation of waters that give rise to the vibrational peak seen in the VSFG spectra.

3.2.1. Free energy of ion complex formation

Consider the structure of the Na_2CO_3 ion complex near a liquid interface. Since two Na^+ cations associate with a single CO_3^{2-} anion, two cation-anion distances, r_1 and r_2 are required to describe the complex. Moreover, the cations may become correlated through direct cation–cation interactions or through solvent mediated interactions where some configurations of the Na_2CO_3 complex are more favorably solvated than others, requiring the specification of the cation angular displacement, $\theta_{\mathrm{NaCNa}} = \arccos(\hat{\mathbf{r}}_1 \cdot \hat{\mathbf{r}}_2)$, where $\hat{\mathbf{r}}$ is the unit vector associated with the vector $\mathbf{r}$. The CO_3^{2-} anion is planar and may exhibit preferential alignment with respect to the interface. This alignment can be captured by the angle $\theta_{\mathrm{CO_3}}$ between the normal axis to the carbonate plane and the normal to the interface. These coordinates are show in Fig. 4(A).

Fig. 5 shows the two-dimensional free energy as a function of the two anion–cation separation distances $F(r_1, r_2)$, of the Na_2CO_3 complex in the bulk and interface chemical environments. Similar to the dissociation of simple ion pairs, each cation shows two minima. The most stable configuration is the contact ion pair (CP) at $r_{1/2} < 4.5$ Å, where the sodium ion is in direct contact with the anion. The second minimum is the metastable solvent-separated ion pair (SSIP) at $4.5 < r_{1/2} < 7$ Å, where the sodium remains near the carbonate anion, with a water molecule separating them. Finally, beyond $r_{1/2} > 7$ Å, the free energy surface plateaus, yielding the dissociated (D) state where the two ions are no longer correlated. These three ion-pairing states are shown schematically in Fig. 4(B).

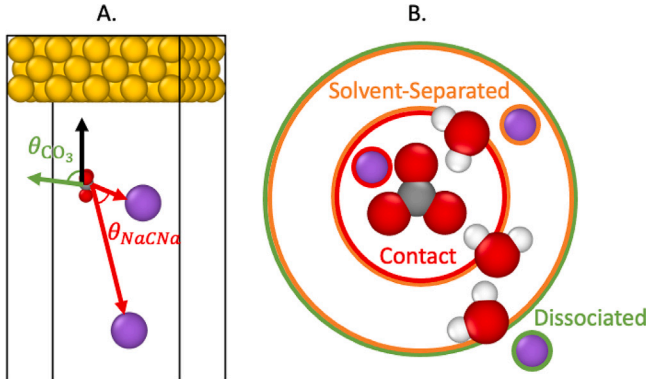

Fig. 4. (A) MD Snapshot of ions and electrodes showing the carbonate alignment angle, $\theta_{\mathrm{CO_3}}$, (green) and cation angular displacement, θ_{NaCNa}, (red). Explicit waters were included in MD simulation but are omitted from this snapshot for clarity. (B) Schematic of sodium cations (purple spheres) in contact ($r \leq 4.5$ Å, red outline), solvent-separated ($4.5 < r \leq 7$ Å, orange outline) and dissociated ($r < 7$ Å, green outline) states. Representative water molecules are shown.

Near electrode interfaces, the three distinct states are unchanged, but their relative stability is modified. In particular, the dissociated and solvent-separated states are destabilized relative to the CP minimum. While the magnitude of this effect varies in the different interfacial environments, the direction of the effect is conserved. To better compare free energies across different chemical environments, we compute 1D free energy curves for one cation, conditioned on the ion-pairing state of the other

$$F(r_1 | r_2 \in X) \equiv -k_B T \log\left[\int_X dr_2 e^{-\frac{F(r_1,r_2)}{k_B T}}\right] \quad (2)$$

where $X \in \{\mathrm{Contact}, \mathrm{Solvent-Separated}, \mathrm{Dissociated}\}$ is the ion-pairing state of cation 2, which we call the auxiliary cation to distinguish it from the probe cation 1.

These conditional free energy curves in Fig. 6, show that in all chemical environments, the probe cation is sensitive to the ion pairing state of the auxiliary cation — increasing as the auxiliary cation dissociates from CO_3^{2-}. In bulk water, the free energy penalty of moving a

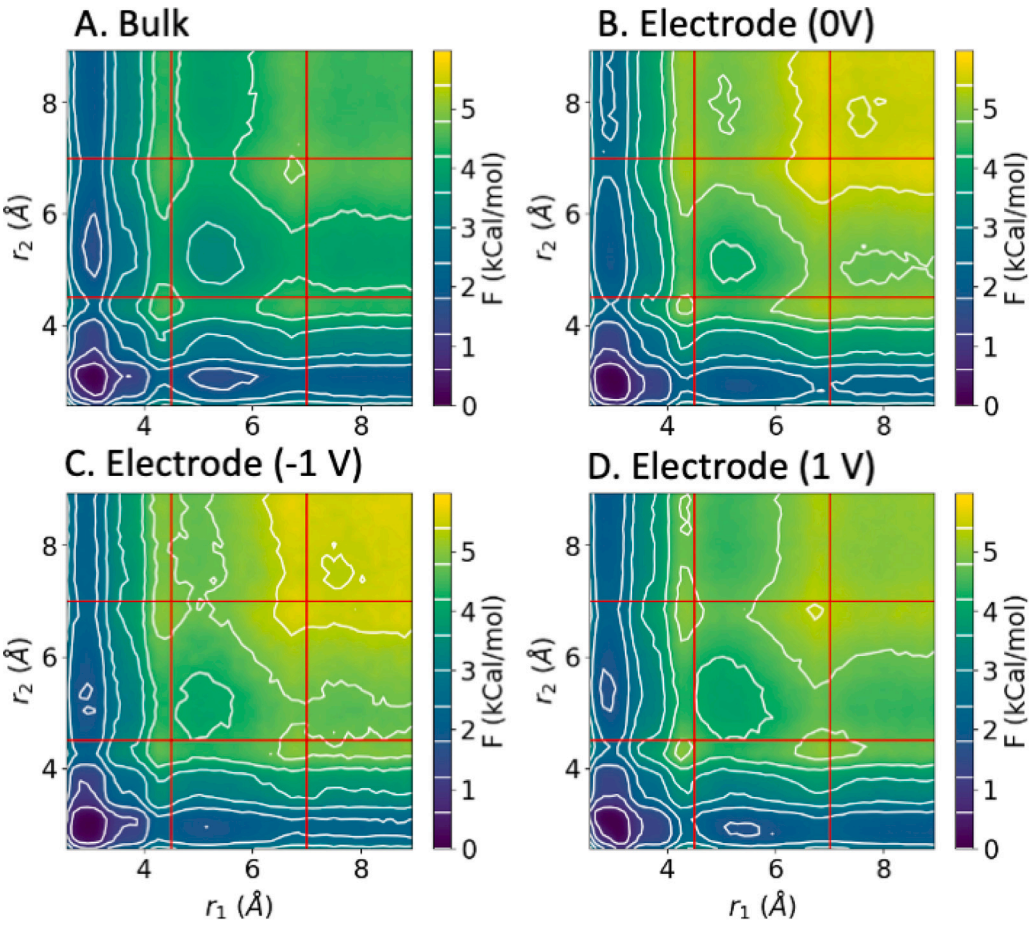

Fig. 5. Two dimensional Free Energy Surfaces for the dissociation of Na_2CO_3 ion complex, in (A) bulk water, (B) near a neutral electrode interface, (C) near an anode interface at −1 V and (D) near a cathode interface at 1 V. White contours are separated by $k_BT = 0.598$ kCal/mol at $T = 300$ K. Red lines indicate the cutoff radii $r = 4.5$ Å and $r = 7$ Å defining the contact, solvent-separated and dissociated states.

cation from the contact to solvent-separated state when the other Na^+ is in contact with CO_3^{2-} is $4.5\,k_BT$ and increases to $5.1\,k_BT$ and $5.5\,k_BT$ when the auxiliary ion is in the solvent-separated and dissociated states respectively. This net $1\,k_BT$ destabilization of the contact state relative to the solvent-separated minimum when a second cation is placed near the anion can be explained by the direct Coulomb repulsion between the two cations — agreeing with the expectation of the change in potential energy of $1\,k_BT$ due to placing an additional +1 charge on the central carbon of CO_3^{2-}.

As ions approach an electrode interface, both the free energy to dissociate an ion pair and the magnitude of the auxiliary ion effects on dissociation free energy increase. The increased free energy cost of ion dissociation can be partially attributed to the volume excluded by the electrode interface. In bulk water, when Na^+ is a distance r away from CO_3^{2-}, it can isotropically access every point in a sphere of that radius. When carbonate approaches an interface, part of this sphere would fall within the electrode, which excludes Na^+ from these regions. As a result, the set of configurations consistent with a Na-C distance is truncated by the electrode, leading to a net destabilization of the dissociated state.

This picture is modified slightly near charged electrode interfaces. When CO_3^{2-} is near the cathode, the negatively charged electrode attracts Na^+ cations bringing them closer to the anion, further penalizing ion dissociation. Near an anode, the opposite occurs, with the positively charged electrode repelling Na^+ away from CO_3^{2-}, slightly mitigating the excluded volume effect. This destabilization does not explain the increase in auxiliary ion effect. Near a neutral electrode, the free energy cost of moving Na^+ from the contact to solvent-separated minimum increases from $5.25\,k_BT$ to $6.5\,k_BT$ and finally $7k_BT$ when the auxiliary cation is in the contact, solvent-separated and dissociated state respectively. The net auxiliary ion effect of $1.75\,k_BT$ is nearly double what is seen in bulk water and cannot be explained by direct Coulomb repulsion between cations. This discrepancy suggests that the cations become more correlated near the interface due to a change in solvation near the interface.

Finally, consider moving the CP-CP complex into van der Waal's contact with electrodes at different applied voltages. Similarly to the 1D PMF's of the ion-complexes considered in Fig. 6, we define the one dimensional Free Energy of moving the CP-CP complex as

$$\frac{F(z)}{k_BT} \equiv \log\left[\int d\boldsymbol{r}_{c_1}\int d\boldsymbol{r}_{c_2}\int d\boldsymbol{r}_{\boldsymbol{a}}\Theta_{CP}(|r_a - r_{c_1}|)\Theta_{CP}(|r_a - r_{c_2}|)\delta(z_a - z)P(\boldsymbol{r}_{c_1},\boldsymbol{r}_{c_2},\boldsymbol{r}_{\boldsymbol{a}})\right], \tag{3}$$

where $\boldsymbol{r}_{c_i}$ is the position of the ith cation, $\boldsymbol{r}_{\boldsymbol{a}}$ and z_a are the position and distance of the anion from the electrode respectively, $\Theta_{CP}(r)$ is the indicator function for the contact ion pair which takes the value 1 if $r < r_{CP}$ and 0 otherwise, δ is the Dirac delta function and P is the probability of each configuration in the unbiased ensemble. This analysis, shown in Fig. 7, quantifies the enhancement or depletion of the most stable configuration of the ion-complex as a function of applied electric field. We see that the CP-CP ion complex shows no statistically significant sensitivity to the electrode charge. For bare ions, the effect of applied voltage on the FES is weak [90], as the applied electric fields are ~1-2 orders of magnitude smaller than the large electric field fluctuations experienced by the ions in water ($\Delta E \sim V/$Å). It is

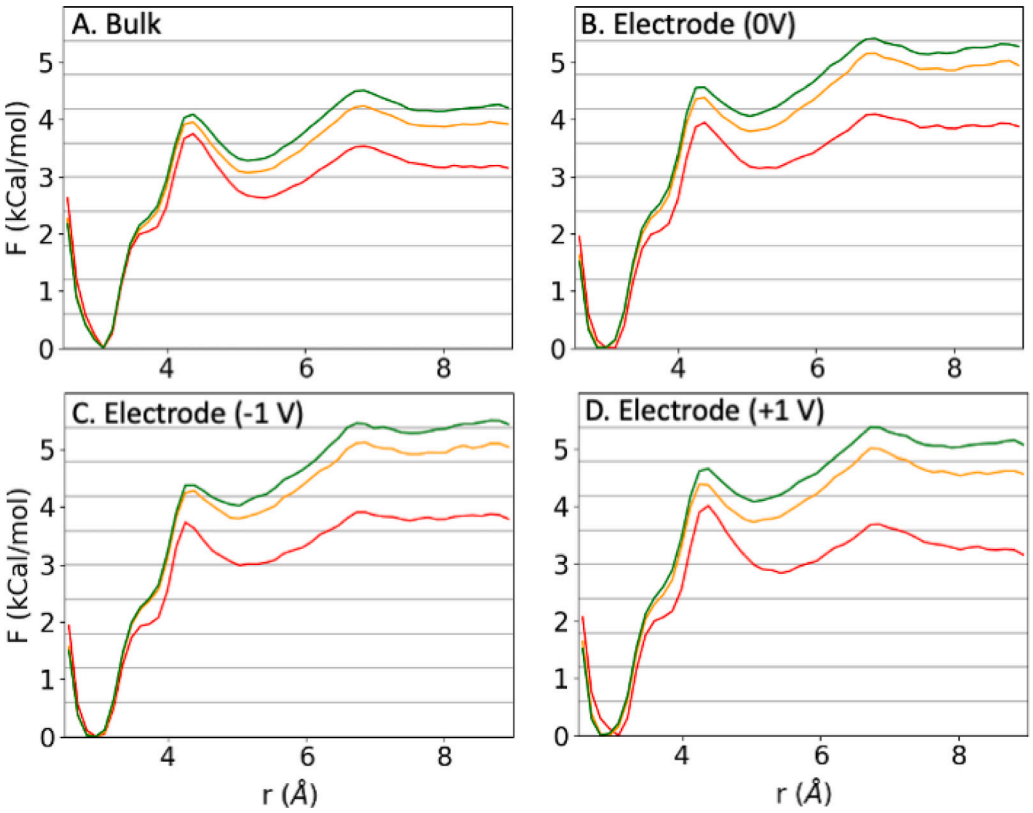

Fig. 6. Conditional ion dissociation free energy curves when the carbonate anion is (A) in bulk liquid, (B) near a neutral electrode interface, (C) near an anode, and (D) near a cathode. In each plot Free energies are computed for one sodium cation when the other cation is in contact with (red), solvent-separated from (orange), or dissociated from (green) the carbonate anion. Horizontal lines are spaced by $k_B T = 0.598$ kCal/mol at $T = 300$ K for reference. The Free Energy slices are shifted to align their minimum at the contact ion pair.

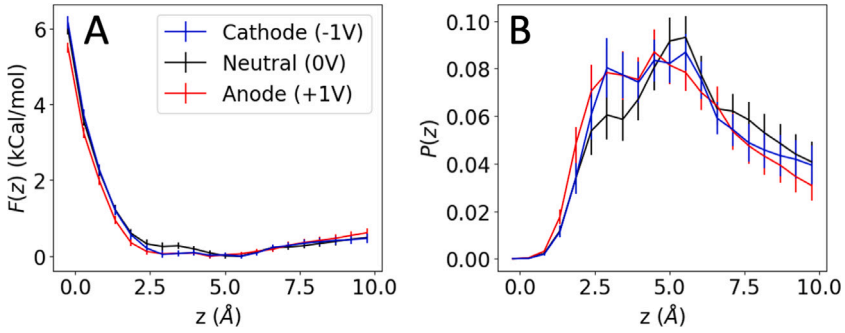

Fig. 7. (A) Free Energy, and (B) Probability Density, of bringing the Carbonate anion in a CP-CP Ion Complex into van der Waal's contact ($z = 0$ Å) with a cathode (blue), anode(red) and neutral electrode (black).

therefore not surprising that the charge neutral CP-CP complex, with a vanishing dipole moment, will show even weaker sensitivity to the applied field. For such a complex, the effect of the applied electric field only appears at the level of field-quadrupole or field-induced dipole interactions, which are much weaker than the field-charge effects that drive bare ions.

3.2.2. Interfacial orientation of ion complexes

Thus far, we have restricted our attention to the radial degrees of freedom of the ion complex, averaging over θ_{NaCNa} and $\theta_{\mathrm{CO_3}}$. The distributions of these angular coordinates in Fig. 8 show that the orientation statistics of the ion complex are sensitive to both the ion-pairing state of the cations and the type of interface it approaches. In the bulk, Figs. 8A and C show that, as expected, the carbonate ion shows no preferential orientation (solid traces). This changes significantly near an interface. Carbonate in a CP complex aligns orthogonal to electrode interfaces, regardless of the sign or magnitude of their applied potential. This decrease in the coplanar population may arise due to Coulomb repulsion between the negatively charged O atoms in the anion and the image charge induced by the contact paired cations. When a charge approaches a conductor, it induces an image charge of the opposite sign on the surface of the conductor. As a CP complex approaches the anion is simultaneously attracted to its own image charge and repelled by the image charge of the associated cation. While the coplanar configuration maximizes the attractive interaction between carbonate and its own image charges it also maximizes the repulsion from the image charge of the sodium cation. This interpretation is supported by the slight increase in the population of coplanar carbonates near an anode. The

positively charged electrode repels the cation, decreasing its associated image charge and mitigating the drive away from the coplanar configuration. In contrast, SSP complexes show a much weaker alignment bias, and a bistability between orthogonal and co-planar CO_3^{2-}. When the cations are further away from carbonate, the repulsion between their image charge and the anion's is significantly reduced, decreasing the resulting penalty to the coplanar configuration.

The inter-cation angle, θ_{NaCNa}, shows an even more dramatic dependence on the ion-pairing state and the interface. The contact paired complex, Fig. 8.B, shows a bistability between a linear state where the two cations are on opposite sides of the anion and a bent configuration where they are nearly orthogonal. This bent configuration is stabilized by the presence of a water molecule in CO_3^{2-}'s first solvation shell with the oxygen between the two cations. This bistability is present in all chemical environments with a relative stability that depends on electrode charge. When the anion is close to the anode, the positively charged electrode repels the cation, pushing the complex towards the bent configuration. In contrast, forming the bent configuration near the cathode requires the recruitment of a water with its oxygen brought into contact with the negatively charged electrode. The Coulomb repulsion of the stabilizing oxygen therefore decreases the probability of the bent configuration.

The solvent-separated configuration shows markedly different behavior from the contact ion complex. Instead of a bistable conformation, the solvent-separated species shows a broad range of angular displacements with a sharp peak in a highly bent configuration where a shared water molecule separates both cations from CO_3^{2-}. This solvent-separated bent configuration is found in all chemical environments but is significantly enhanced near neutral electrodes and anodes.

3.2.3. Simulated water spectra

Finally, we consider how the vibrational spectrum of water is modified by the presence of the ions and electrode. Our goal is to identify the subpopulation of OH bonds that produces the peak around 3400 cm^{-1} in the experimental VSFG spectrum and why this peak emerges only under an applied potential. We begin this analysis by computing the spectrum of all OH bonds in each of the simulations. We find that under all conditions, the total water spectrum was nearly indistinguishable from that of the pure liquid, since only a very small number of water molecules experience a local environment that differs significantly from the pure liquid. In particular, no spectral feature was observed near 3400 cm^{-1}. In Fig. 9(A), we consider the spectrum of only the water molecules within one Debye length (8 Å) of the anode. These interfacial water spectra do not differ significantly from the bulk, and lack any feature in the 3400 cm^{-1} region. Repeating this analysis for only the first water layer, within 3 Å of the interface, also produced spectra that did not differ substantially from the bulk. The experimental signal therefore cannot be attributed simply to water near the interface.

Next, we consider only water molecules in the first solvation shell of the anion. Previous simulations of Raman spectroscopy in halide solutions found that ion specific spectral features could be attributed primarily to these waters closest to the ion [63]. In order to define the first solvation shell, we consider the hydrogen–carbon (HC) radial distribution function, $g(r_{HC})$ in Fig. 9(C). Under all simulation conditions, the $g(r_{HC})$ shows a local minimum at 3.5 Å defining the cutoff for first solvation shell hydrogens. Computing the spectrum of only these waters in Fig. 9(B), we see a clear spectral peak emerges below 3400 cm^{-1}. We therefore assign the experimental peak to OH bonds in the first solvation shall of Carbonate. This assignment can be further validated by selecting the OH bonds with a vibration frequency $\leq$ 3400 cm^{-1} and computing $g(r_{HC})$ for this "High Field" sub-population. In Fig. 9(C) we plot the difference between this sub-population $g(r_{HC})$ and that of all hydrogens for each simulation condition, confirming that the spectral peak can indeed be attributed primarily to the first solvation shell with a small contribution from the second solvation shell. This figure is a statistical assignment of the spectral peak, quantitatively identifying the water sub-population that is overrepresented in the spectral region of interest.

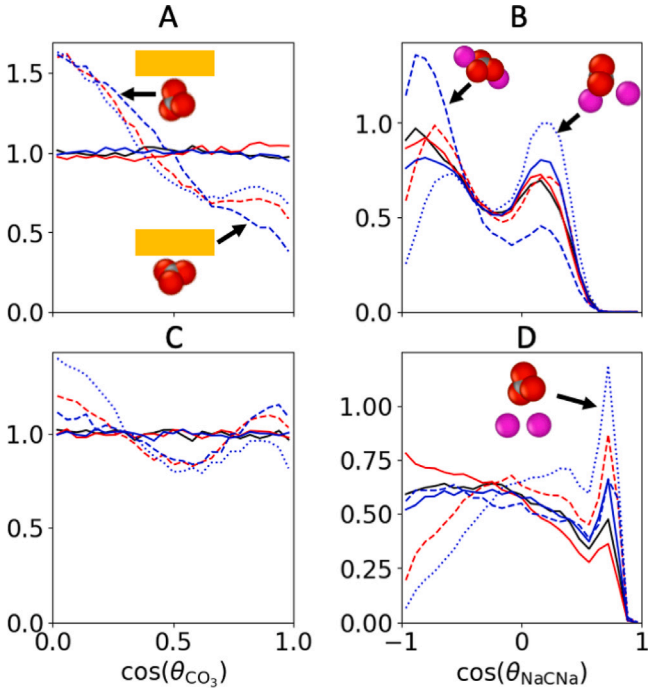

Fig. 8. (Left) Histograms of Carbonate orientation, θ_{CO_3} when both Na cations are (A) in contact with or (c) solvent-separated from CO_3^{2-}. (Right) Histograms of the angular displacement θ_{NaCNa} of the two Na cations when both Na cations are (B) in contact with or (D) solvent-separated from CO_3^{2-}. Inset figures show sample configurations from different sub-population peaks in the histogram. In all plots, results are shown for CO_3^{2-} in bulk water (solid black); a cell with no applied potential in the bulk (solid red), and near the electrode (dashed red); and in a cell with a 1 V applied potential in the bulk (solid blue), near the cathode (dotted blue), and near the anode (dashed blue).

While this spectral peak is present in all simulation conditions, its characteristics differ between the bulk (solid lines) and interfaces (dashed lines). When a carbonate is near the interface, the primary spectral peak is red-shifted by ~50 cm^{-1}. This shift indicates that the first solvation shell OH bonds typically experience larger fields when carbonate is near an electrode than in the bulk, due to the presence of image charge effects. In addition, we see the presence of a blue shifted feature near 3700 cm^{-1} when Carbonate is near the interface. The presence of this low-field sub-population of water may indicate the formation of a vacuum region and a partial dewetting of the ion complex itself or of the interface near the ion complex.

Although we have assigned the water sub-population responsible for the experimental peak, this population is present in similar quantities across all simulation conditions, including bulk water and near a neutral electrode. It remains to show why this peak only emerges in VSFG under an applied potential. Sum frequency generation is a surface-sensitive technique that is sensitive only to regions where inversion symmetry is broken. Therefore, if the orientational distribution of a collection of OH bonds contributing to a spectral feature is inversion symmetric, that feature will not appear in the VSFG spectrum. Noah-Vanhoucke et al. [67] have shown that this breaking of inversion symmetry in water is well-described by considering only the projection of the OH bonds along the z direction orthogonal to the interface. In Fig. 9(D), we consider this orientational distribution for different simulation conditions. In the pure water simulation (black trace), the OH bond distribution is isotropic, indicating that bulk water will not contribute appreciably to the VSFG spectrum — even if it has a sub-population of first solvation shell waters in the spectral range of interest. The orientation distribution near a neutral electrode(red

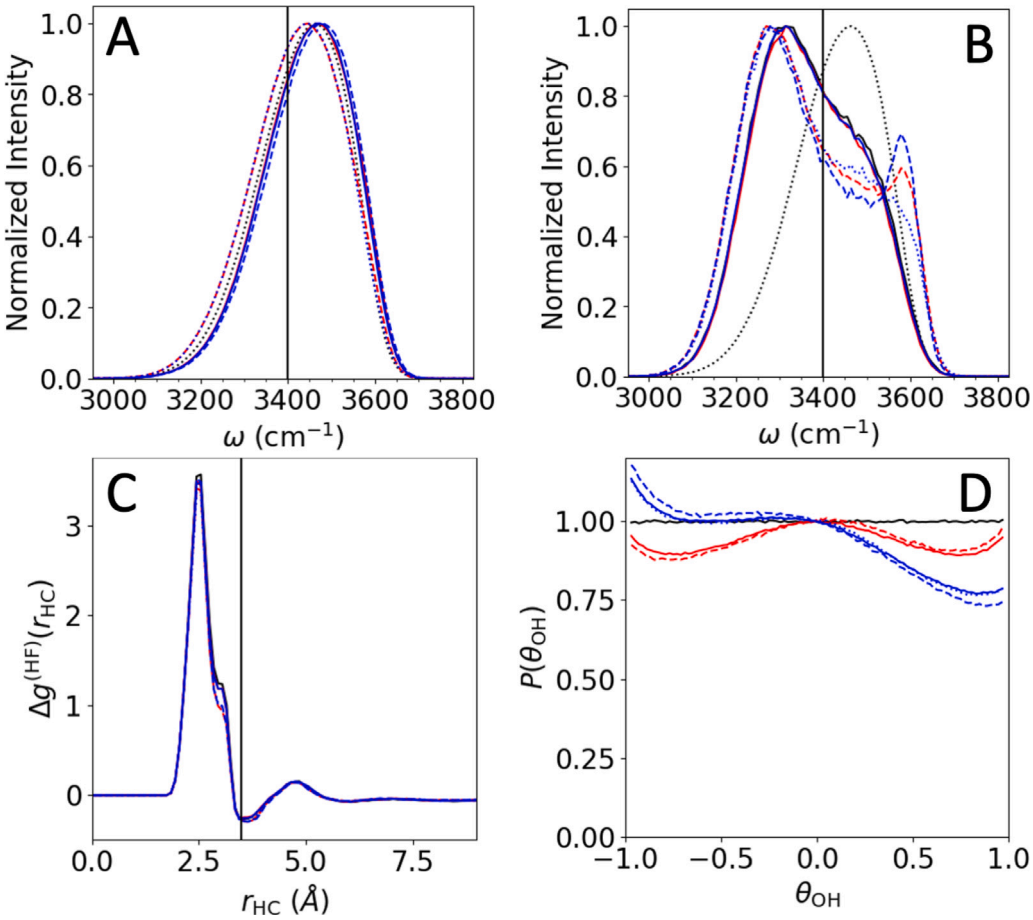

Fig. 9. (A, B) Simulated vibrational spectra of water OH stretch. The dotted black line shows the bulk water spectrum. Vertical black line at $\omega = 3400\ cm^{-1}$ indicates the location of the experimental peak, and the maximum frequency (minimum field) that defines the High Field water population. The remaining traces show the spectrum of OH bonds (A) within a Debye length of the cathode and (B) within the first solvation shell of carbonate ($r_{HC} < 3.5$ Å), conditioned on CO_3^{2-} being in different chemical environments. (C) Difference in radial distribution function for High Field Hydrogens, $\omega < 3400\ cm^{-1}$ compared to all Hydrogens in the system. Vertical line in (C) at $r_{HC} = 3.5$ Å indicate the cut-off for first solvation shell Hydrogens. (D) The distribution of OH bond alignments with respect to the electrode interface. Trace colors as described in Fig. 8. *In all plots, results are shown for CO_3^{2-} in bulk water (solid black); a cell with no applied potential in the bulk (solid red), and near the electrode (dashed red); and in a cell with a 1 V applied potential in the bulk (solid blue), near the cathode (dotted blue), and near the anode (dashed blue).*

traces), while anisotropic is still inversion symmetric and thus will also not contribute a VSFG signal. When an external field is applied, water molecules near the interface will align in response to the applied field, breaking inversion symmetry and therefore contributing to the VSFG spectrum. The role of the external field is therefore to align the waters in carbonate's solvation shell, rendering them VSFG active and producing the observed experimental signal. A similar mechanism of a water population that becomes more aligned as an external parameter is varied has been previously demonstrated in the simulation of vibrational SFG spectra of dilute ionic solutions [68], where the alignment of water molecules at the interface increased with anion size. This interpretation also allows us to understand the red-shift of the new spectral peak with increasing applied voltage seen in Fig. 1, in spite of the insensitivity of the theoretical electric field statistics in Fig. 9 to the applied voltage. Specifically, as the alignment of the spectral feature at 3300 cm^{-1} increases, its amplitude increases. The overlap of this peak with a bulk water peak around 3500 cm^{-1} would then produce a red-shift as the amplitude of the lower frequency peak increases.

Fig. 10 shows a typical configuration from MD simulations highlighting the water molecules characteristic of the VSFG peak at 3400 cm^{-1}. This sub-population of water molecules is found in the first solvation shell of a CO_3^{2-} anion near the interface and displays a clear preferential alignment of their OH bonds, breaking inversion symmetry and making their vibrations visible in the VSFG spectrum. This prediction of unique water vibrations in the first solvation shell of CO_3^{2-} is consistent with 2DIR studies in bulk water [97]. The proximity to carbonate leads to a large electric field along the OH bonds, producing the observed red shift in the vibrational frequency relative to bulk water, while the charged interface leads to the observed alignment. In addition, the ion complex is shown in its most probable configuration near the cathode. The Na^+ cations are both in contact with the anion on opposite sides with the plane of CO_3^{2-} orthogonal to the interface. This snapshot should not be understood as an exclusive assignment of the peak, with every water molecule contributing to this spectral region being found in a nearly identical configuration. Instead, it represents the most common structure contributing to the emergent spectral peak, highlighting the conformational properties statistically associated with this spectral region. We note that within this configuration there exist multiple aligned water molecules between the ion pair complex and the surface, which may serve as a proton donor during the coupled proton/electron transfer required for CO_2 activation. However, future studies will be required to evaluate the effect of the observed interfacial water alignment on the CO_2R reaction kinetics.

4. Conclusion

We have used vibrational sum frequency generation spectroscopy to study the water structure at the interface of carbonate electrolyte solutions and a gold electrode under applied potentials relevant to

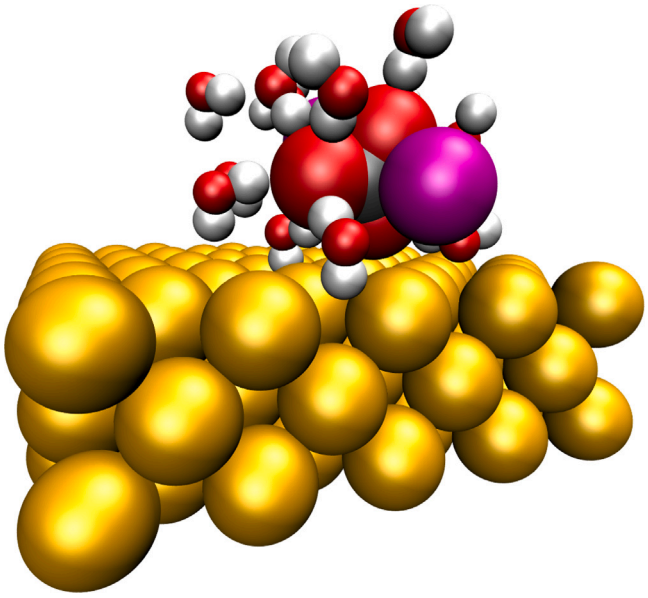

Fig. 10. MD snapshot showing the aligned first solvation shell water molecules near the cathode that give rise to the peak in the VSFG spectrum at 3400 cm^{-1}.

CO_2R. We observed a peak at around 3400 cm^{-1} at catalytic potentials in the presence of carbonate anions, and this peak is assigned to a sodium-carbonate ion complex, which is over-represented near the interface. The peak is much more prominent for Na_2CO_3 than Cs_2CO_3 suggesting this peak is not only anion specific but also cation specific. Using molecular dynamics simulations, we link these observed spectral changes to the impact of carbonate on the potential-dependent alignment of interfacial water and the creation of a solvent-separated sodium-carbonate ion pair. The peak around 3400 cm^{-1} is assigned to water molecules in the first solvation shell of a CO_3^{2-} anion near the interface, which show a preferential orientation of their OH bonds. This orientation disrupts the inversion symmetry, leading to the visibility of their vibrations in the VSFG spectrum. The solvent-separated configuration of the ion pair shows markedly different behavior from the contact ion complex. Instead of a bistable conformation, the solvent-separated ion pairs displays a broad range of angular displacements with a sharp peak in a highly bent configuration with the two sodium ions separated from one another by one water molecule. This solvent-separated bent configuration is found in all chemical environments but is significantly enhanced near electrode surface. These findings reveal ion pairing plays an important role in the structure and alignment of interfacial water under conditions relevant for electrochemical catalysis, including CO_2R and lays the groundwork for future studies to further consider the impact of these structures on the kinetics and mechanisms of electrochemical reactions.

CRediT authorship contribution statement

Amro Dodin: Writing – review & editing, Writing – original draft, Methodology, Formal analysis. **Gang-Hua Deng:** Writing – review & editing, Writing – original draft, Formal analysis, Data curation, Conceptualization. **Jaclyn A. Rebstock:** Writing – review & editing, Formal analysis. **Quansong Zhu:** Writing – review & editing, Formal analysis. **David T. Limmer:** Writing – review & editing, Writing – original draft, Supervision, Funding acquisition, Formal analysis, Conceptualization. **L. Robert Baker:** Writing – review & editing, Writing – original draft, Supervision, Funding acquisition, Formal analysis, Conceptualization.

Declaration of competing interest

The authors declare that they have no known competing financial interests or personal relationships that could have appeared to influence the work reported in this paper.

Data availability

Data will be made available on request.

Acknowledgments

VSFG measurements were supported by the Condensed Phase and Interfacial Molecular Science Program (CPIMS), in the Chemical Sciences Geosciences and Biosciences Division of the Office of Basic Energy Sciences of the U.S. Department of Energy under Contract No. DE-SC0020977. The theory and simulations were supported by the Condensed Phase and Interfacial Molecular Science Program (CPIMS), in the Chemical Sciences Geosciences and Biosciences Division of the Office of Basic Energy Sciences of the U.S. Department of Energy under Contract No. DE-AC02-05CH11231.

Appendix A. Supplementary data

Supplementary material related to this article can be found online at https://doi.org/10.1016/j.apsusc.2024.160345.

References

[1] J. Wu, Y. Huang, W. Ye, Y. Li, CO2 reduction: From the electrochemical to photochemical approach, Adv. Sci. 4 (11) (2017) 1700194.
[2] S. Nitopi, E. Bertheussen, S.B. Scott, X. Liu, A.K. Engstfeld, S. Horch, B. Seger, I.E.L. Stephens, K. Chan, C. Hahn, J.K. Nørskov, T.F. Jaramillo, I. Chorkendorff, Progress and perspectives of electrochemical CO2 reduction on copper in aqueous electrolyte, Chem. Rev. 119 (12) (2019) 7610–7672, PMID: 31117420.
[3] X. Zhang, S.-X. Guo, K.A. Gandionco, A.M. Bond, J. Zhang, Electrocatalytic carbon dioxide reduction: from fundamental principles to catalyst design, Mat. Today Adv. 7 (2020) 100074.
[4] R. Casebolt, K.W. Kimura, K. Levine, J.A. Cimada DaSilva, J. Kim, T.A. Dunbar, J. Suntivich, T. Hanrath, Effect of electrolyte composition and concentration on pulsed potential electrochemical CO2 reduction, ChemElectroChem 8 (4) (2021) 681–688.
[5] M.R. Thorson, K.I. Siil, P.J.A. Kenis, Effect of cations on the electrochemical conversion of CO2 to CO, J. Electrochem. Soc. 160 (1) (2012) F69.
[6] S. Verma, X. Lu, S. Ma, R.I. Masel, P.J.A. Kenis, The effect of electrolyte composition on the electroreduction of CO2 to CO on Ag based gas diffusion electrodes, Phys. Chem. Chem. Phys. 18 (2016) 7075–7084.
[7] J. Resasco, Y. Lum, E. Clark, J.Z. Zeledon, A.T. Bell, Effects of anion identity and concentration on electrochemical reduction of CO2, ChemElectroChem 5 (7) (2018) 1064–1072.
[8] G. Marcandalli, A. Goyal, M.T.M. Koper, Electrolyte effects on the faradaic efficiency of CO2 reduction to CO on a gold electrode, ACS Catal. 11 (9) (2021) 4936–4945, PMID: 34055454.
[9] M. Moura de Salles Pupo, R. Kortlever, Electrolyte effects on the electrochemical reduction of CO2, ChemPhysChem 20 (22) (2019) 2926–2935.
[10] Q. Zhu, S.K. Wallentine, G.-H. Deng, J.A. Rebstock, L.R. Baker, The solvation-induced onsager reaction field rather than the double-layer field controls CO2 reduction on gold, JACS Au 2 (2) (2022) 472–482.
[11] A. Frumkin, Influence of cation adsorption on the kinetics of electrode processes, Trans. Faraday Soc. 55 (1959) 156–167.
[12] Y. Hori, S. Suzuki, Electrolytic reduction of carbon dioxide at mercury electrode in aqueous solution, Bull. Chem. Soc. Jpn. 55 (3) (1982) 660–665.
[13] J. Li, X. Li, C.M. Gunathunge, M.M. Waegele, Hydrogen bonding steers the product selectivity of electrocatalytic CO reduction, Proc. Natl. Acad. Sci. 116 (19) (2019) 9220–9229.
[14] J.A. Rebstock, Q. Zhu, L.R. Baker, Comparing interfacial cation hydration at catalytic active sites and spectator sites on gold electrodes: understanding structure sensitive CO 2 reduction kinetics, Chem. Sci. 13 (25) (2022) 7634–7643.
[15] D.T. Limmer, A.P. Willard, P.A. Madden, D. Chandler, Water exchange at a hydrated platinum electrode is rare and collective, J. Phys. Chem. C 119 (42) (2015) 24016–24024.
[16] T. Ludwig, J.A. Gauthier, K.S. Brown, S. Ringe, J.K. Nørskov, K. Chan, Solvent–adsorbate interactions and adsorbate-specific solvent structure in carbon dioxide reduction on a stepped Cu surface, J. Phys. Chem. C 123 (10) (2019) 5999–6009.

[17] M.C. Monteiro, F. Dattila, B. Hagedoorn, R. García-Muelas, N. López, M.T. Koper, Absence of CO2 electroreduction on copper, gold and silver electrodes without metal cations in solution, Nat. Catal. 4 (8) (2021) 654–662.

[18] M.R. Singh, Y. Kwon, Y. Lum, J.W. Ager III, A.T. Bell, Hydrolysis of electrolyte cations enhances the electrochemical reduction of CO2 over Ag and Cu, J. Am. Chem. Soc. 138 (39) (2016) 13006–13012.

[19] L.D. Chen, M. Urushihara, K. Chan, J.K. Nørskov, Electric field effects in electrochemical CO2 reduction, ACS Catal. 6 (10) (2016) 7133–7139.

[20] J.-M. Savéant, Effect of ion pairing on the mechanism and rate of electron transfer. Electrochemical aspects, J. Phys. Chem. B 105 (37) (2001) 8995–9001.

[21] Y. Marcus, G. Hefter, Ion pairing, Chem. Rev. 106 (11) (2006) 4585–4621, PMID: 17091929.

[22] N.F.A. van der Vegt, K. Haldrup, S. Roke, J. Zheng, M. Lund, H.J. Bakker, Water-mediated ion pairing: Occurrence and relevance, Chem. Rev. 116 (13) (2016) 7626–7641, PMID: 27153482.

[23] J.A. Kattirtzi, D.T. Limmer, A.P. Willard, Microscopic dynamics of charge separation at the aqueous electrochemical interface, Proc. Natl. Acad. Sci. 114 (51) (2017) 13374–13379.

[24] M. Fleischmann, I.R. Hill, The observation of solvated metal ions in the double layer region at silver electrodes using surface enhanced raman scattering, J. Electroanal. Chem. 146 (2) (1983) 367–376.

[25] S.Z. Zou, Y.X. Chen, B.W. Mao, B. Ren, Z.Q. Tian, SERS studies on electrode/electrolyte interfacial water I. Ion effects in the negative potential region, J. Electroanal. Chem. 424 (1) (1997) 19–24.

[26] N. Bjerrum, 1926. 7, 9.

[27] R.M. Fuoss, Distribution of ions in electrolytic solutions, Trans. Faraday Soc. 50 (1934) 967.

[28] Y. Marcus, G. Hefter, Ion pairing, Chem. Rev. 106 (11) (2006) 4585–4621.

[29] S. Arrhenius, Über die Dissociation der in Wasser gelösten Stoffe, Z. Phys. Chem. 1U (1) (1887) 631–648, Publisher: De Gruyter (O).

[30] K. Ma, J. Forsman, C.E. Woodward, Influence of ion pairing in ionic liquids on electrical double layer structures and surface force using classical density functional approach, J. Chem. Phys. 142 (17) (2015) 174704.

[31] J. Lyklema, Quest for ion–ion correlations in electric double layers and overcharging phenomena, Adv. Colloid Interface Sci. 147–148 (2009) 205–213.

[32] V. Venkateshwaran, S. Vembanur, S. Garde, Water-mediated ion–ion interactions are enhanced at the water vapor–liquid interface, Proc. Natl. Acad. Sci. 111 (24) (2014) 8729–8734, Publisher: Proceedings of the National Academy of Sciences.

[33] F. Jiménez-Ángeles, K.J. Harmon, T.D. Nguyen, P. Fenter, M. Olvera de la Cruz, Nonreciprocal interactions induced by water in confinement, Phys. Rev. Res. 2 (4) (2020) 043244.

[34] S.W. Devlin, S. Jamnuch, Q. Xu, A.A. Chen, J. Qian, T.A. Pascal, R.J. Saykally, Agglomeration drives the reversed fractionation of aqueous carbonate and bicarbonate at the air–water interface, J. Am. Chem. Soc. 145 (41) (2023) 22384–22393.

[35] R.K. Lam, J.W. Smith, A.M. Rizzuto, O. Karslıoğlu, H. Bluhm, R.J. Saykally, Reversed interfacial fractionation of carbonate and bicarbonate evidenced by X-ray photoemission spectroscopy, J. Chem. Phys. 146 (9) (2017) 094703.

[36] S. Wallentine, S. Bandaranayake, S. Biswas, L.R. Baker, Plasmon-resonant vibrational sum frequency generation of electrochemical interfaces: Direct observation of carbon dioxide electroreduction on gold, J. Phys. Chem. A 124 (39) (2020) 8057–8064, PMID: 32846085.

[37] S. Wallentine, S. Bandaranayake, S. Biswas, L.R. Baker, Direct observation of carbon dioxide electroreduction on gold: Site blocking by the stern layer controls CO2 adsorption kinetics, J. Phys. Chem. Lett. 11 (19) (2020) 8307–8313, PMID: 32946241.

[38] G.-H. Deng, Q. Zhu, J. Rebstock, T. Neves-Garcia, L.R. Baker, Direct observation of bicarbonate and water reduction on gold: understanding the potential dependent proton source during hydrogen evolution, Chem. Sci. 14 (17) (2023) 4523–4531.

[39] A.P. Thompson, H.M. Aktulga, R. Berger, D.S. Bolintineanu, W.M. Brown, P.S. Crozier, P.J. in 't Veld, A. Kohlmeyer, S.G. Moore, T.D. Nguyen, R. Shan, M.J. Stevens, J. Tranchida, C. Trott, S.J. Plimpton, LAMMPS - a flexible simulation tool for particle-based materials modeling at the atomic, meso, and continuum scales, Comp. Phys. Comm. 271 (2022) 108171.

[40] G.M. Torrie, J.P. Valleau, Nonphysical sampling distributions in Monte Carlo free-energy estimation: Umbrella sampling, J. Comput. Phys. 23 (2) (1977) 187–199.

[41] J. Kästner, Umbrella sampling, WIREs Comput. Mol. Sci. 1 (6) (2011) 932–942.

[42] S. Kumar, J.M. Rosenberg, D. Bouzida, R.H. Swendsen, P.A. Kollman, The weighted histogram analysis method for free-energy calculations on biomolecules. I. The method, J. Comput. Chem. 13 (8) (1992) 1011–1021.

[43] S. Kumar, J.M. Rosenberg, D. Bouzida, R.H. Swendsen, P.A. Kollman, Multidimensional free-energy calculations using the weighted histogram analysis method, J. Comput. Chem. 16 (11) (1995) 1339–1350.

[44] M. Souaille, B. Roux, Extension to the weighted histogram analysis method: combining umbrella sampling with free energy calculations, Comput. Phys. Comm. 135 (1) (2001) 40–57.

[45] A. Grossfield, WHAM: the weighted histogram analysis method, 2002, URL http://membrane.urmc.rochester.edu/wordpress/?page_id=126.

[46] J.I. Siepmann, M. Sprik, Influence of surface topology and electrostatic potential on water/electrode systems, J. Chem. Phys. 102 (1) (1995) 511–524.

[47] S.K. Reed, O.J. Lanning, P.A. Madden, Electrochemical interface between an ionic liquid and a model metallic electrode, J. Chem. Phys. 126 (8) (2007) 084704.

[48] L. Scalfi, D.T. Limmer, A. Coretti, S. Bonella, P.A. Madden, M. Salanne, B. Rotenberg, Charge fluctuations from molecular simulations in the constant-potential ensemble, Phys. Chem. Chem. Phys. 22 (19) (2020) 10480–10489.

[49] L.J.V. Ahrens-Iwers, M. Janssen, S.R. Tee, R.H. Meißner, ELECTRODE: An electrochemistry package for atomistic simulations, J. Chem. Phys. 157 (8) (2022) 084801.

[50] G. Lamoureux, B. Roux, Modeling induced polarization with classical Drude oscillators: Theory and molecular dynamics simulation algorithm, J. Chem. Phys. 119 (6) (2003) 3025–3039.

[51] J.A. Lemkul, J. Huang, B. Roux, A.D.J. MacKerell, An empirical polarizable force field based on the classical drude oscillator model: Development history and recent applications, Chem. Rev. 116 (9) (2016) 4983–5013.

[52] A. Dequidt, J. Devémy, A.A.H. Pádua, Thermalized drude oscillators with the LAMMPS molecular dynamics simulator, J. Chem. Inf. Model. 56 (1) (2016) 260–268, Publisher: American Chemical Society.

[53] T.D. Archer, S.E.A. Birse, M.T. Dove, S.A.T. Redfern, J.D. Gale, R.T. Cygan, An interatomic potential model for carbonates allowing for polarization effects, Phys. Chem. Miner. 30 (7) (2003) 416–424.

[54] F. Bruneval, D. Donadio, M. Parrinello, Molecular dynamics study of the solvation of calcium carbonate in water, J. Phys. Chem. B 111 (42) (2007) 12219–12227.

[55] H. Du, J. Liu, O. Ozdemir, A.V. Nguyen, J.D. Miller, Molecular features of the air/carbonate solution interface, J. Colloid. Interf. Sci. 318 (2) (2008) 271–277.

[56] A. Dodin, P.L. Geissler, Symmetrized drude oscillator force fields improve numerical performance of polarizable molecular dynamics, J. Chem. Theory Comput. 19 (10) (2023) 2906–2917.

[57] R. Car, M. Parrinello, Unified approach for molecular dynamics and density-functional theory, Phys. Rev. Lett. 55 (22) (1985) 2471–2474.

[58] G.J. Martyna, M.L. Klein, M. Tuckerman, Nosé–Hoover chains: The canonical ensemble via continuous dynamics, J. Chem. Phys. 97 (4) (1992) 2635–2643.

[59] W.G. Hoover, Canonical dynamics: Equilibrium phase-space distributions, Phys. Rev. A 31 (3) (1985) 1695–1697.

[60] G. Lamoureux, E. Harder, I.V. Vorobyov, B. Roux, A.D. MacKerell, A polarizable model of water for molecular dynamics simulations of biomolecules, Chem. Phys. Lett. 418 (1–3) (2006) 245–249.

[61] H. Kamberaj, R.J. Low, M.P. Neal, Time reversible and symplectic integrators for molecular dynamics simulations of rigid molecules, J. Chem. Phys. 122 (22) (2005) 224114.

[62] J.D. Smith, C.D. Cappa, K.R. Wilson, R.C. Cohen, P.L. Geissler, R.J. Saykally, Unified description of temperature-dependent hydrogen-bond rearrangements in liquid water, Proc. Natl. Acad. Sci. 102 (40) (2005) 14171–14174.

[63] J.D. Smith, R.J. Saykally, P.L. Geissler, The effects of dissolved halide anions on hydrogen bonding in liquid water, J. Am. Chem. Soc. 129 (45) (2007) 13847–13856.

[64] H.J. Bakker, J.L. Skinner, Vibrational spectroscopy as a probe of structure and dynamics in liquid water, Chem. Rev. 110 (3) (2010) 1498–1517.

[65] P.L. Geissler, Water interfaces, solvation, and spectroscopy, Annu. Rev. Phys. Chem. 64 (2013) 317–337.

[66] C.R. Baiz, B. Błasiak, J. Bredenbeck, M. Cho, J.-H. Choi, S.A. Corcelli, A.G. Dijkstra, C.-J. Feng, S. Garrett-Roe, N.-H. Ge, M.W.D. Hanson-Heine, J.D. Hirst, T.L.C. Jansen, K. Kwac, K.J. Kubarych, C.H. Londergan, H. Maekawa, M. Reppert, S. Saito, S. Roy, J.L. Skinner, G. Stock, J.E. Straub, M.C. Thielges, K. Tominaga, A. Tokmakoff, H. Torii, L. Wang, L.J. Webb, M.T. Zanni, Vibrational spectroscopic map, vibrational spectroscopy, and intermolecular interaction, Chem. Rev. 120 (15) (2020) 7152–7218.

[67] J. Noah-Vanhoucke, J.D. Smith, P.L. Geissler, Toward a simple molecular understanding of sum frequency generation at air-water interfaces, J. Phys. Chem. B 113 (13) (2009) 4065–4074.

[68] J. Noah-Vanhoucke, J.D. Smith, P.L. Geissler, Statistical mechanics of sum frequency generation spectroscopy for the liquidâvapor interface of dilute aqueous salt solutions, Chem. Phys. Lett. 470 (1) (2009) 21–27.

[69] Y. Ni, J.L. Skinner, Communication: Vibrational sum-frequency spectrum of the air-water interface, revisited, J. Chem. Phys. 145 (3) (2016) 031103.

[70] M.S. Chen, Y. Mao, A. Snider, P. Gupta, A. Montoya-Castillo, T.J. Zuehlsdorff, C.M. Isborn, T.E. Markland, Elucidating the role of hydrogen bonding in the optical spectroscopy of the solvated green fluorescent protein chromophore: Using machine learning to establish the importance of high-level electronic structure, J. Phys. Chem. Lett. 14 (29) (2023) 6610–6619.

[71] Y.R. Shen, V. Ostroverkhov, Sum-frequency vibrational spectroscopy on water interfaces: polar orientation of water molecules at interfaces, Chem. Rev. 106 (4) (2006) 1140–1154.

[72] C. Tian, Y. Shen, Recent progress on sum-frequency spectroscopy, Surf. Sci. Rep. 69 (2–3) (2014) 105–131.

[73] H. Arnolds, M. Bonn, Ultrafast surface vibrational dynamics, Surf. Sci. Rep. 65 (2) (2010) 45–66.

[74] D. Bhattacharyya, P.E. Videla, M. Cattaneo, V.S. Batista, T. Lian, C.P. Kubiak, Vibrational stark shift spectroscopy of catalysts under the influence of electric fields at electrode–solution interfaces, Chem. Sci. 12 (30) (2021) 10131–10149.

[75] H.-F. Wang, W. Gan, R. Lu, Y. Rao, B.-H. Wu, Quantitative spectral and orientational analysis in surface sum frequency generation vibrational spectroscopy (SFG-VS), Int. Rev. Phys. Chem. 24 (2) (2005) 191–256.
[76] E.H. Backus, N. Garcia-Araez, M. Bonn, H.J. Bakker, On the role of fresnel factors in sum-frequency generation spectroscopy of metal–water and metal-oxide–water interfaces, J. Phys. Chem. C 116 (44) (2012) 23351–23361.
[77] P.E. Ohno, H.-f. Wang, F.M. Geiger, Second-order spectral lineshapes from charged interfaces, Nature Commun. 8 (1) (2017) 1032.
[78] A. Montenegro, C. Dutta, M. Mammetkuliev, H. Shi, B. Hou, D. Bhattacharyya, B. Zhao, S.B. Cronin, A.V. Benderskii, Asymmetric response of interfacial water to applied electric fields, Nature 594 (7861) (2021) 62–65.
[79] Y.-C. Wen, S. Zha, X. Liu, S. Yang, P. Guo, G. Shi, H. Fang, Y.R. Shen, C. Tian, Unveiling microscopic structures of charged water interfaces by surface-specific vibrational spectroscopy, Phys. Rev. Lett. 116 (1) (2016) 016101.
[80] P.E. Ohno, H.-f. Wang, F. Paesani, J.L. Skinner, F.M. Geiger, Second-order vibrational lineshapes from the air/water interface, J. Phys. Chem. A 122 (18) (2018) 4457–4464.
[81] K.C. Jena, P.A. Covert, D.K. Hore, The effect of salt on the water structure at a charged solid surface: Differentiating second-and third-order nonlinear contributions, J. Phys. Chem. Lett. 2 (9) (2011) 1056–1061.
[82] G. Gonella, C. Lutgebaucks, A.G. De Beer, S. Roke, Second harmonic and sum-frequency generation from aqueous interfaces is modulated by interference, J. Phys. Chem. C 120 (17) (2016) 9165–9173.
[83] A. Eftekhari-Bafrooei, E. Borguet, Effect of electric fields on the ultrafast vibrational relaxation of water at a charged solid–liquid interface as probed by vibrational sum frequency generation, J. Phys. Chem. Lett. 2 (12) (2011) 1353–1358.
[84] P.E. Ohno, H. Chang, A.P. Spencer, Y. Liu, M.D. Boamah, H.-f. Wang, F.M. Geiger, Beyond the Gouy–Chapman model with heterodyne-detected second harmonic generation, J. Phys. Chem. Lett. 10 (10) (2019) 2328–2334.
[85] P. Xu, A.D. von Rueden, R. Schimmenti, M. Mavrikakis, J. Suntivich, Optical method for quantifying the potential of zero charge at the platinum–water electrochemical interface, Nature Mater. 22 (4) (2023) 503–510.
[86] P. Xu, R. Wang, H. Zhang, V. Carnevale, E. Borguet, J. Suntivich, Cation modifies interfacial water structures on platinum during alkaline hydrogen electrocatalysis, J. Am. Chem. Soc. 146 (4) (2024) 2426–2434.
[87] Y. Tong, F. Lapointe, M. Thämer, M. Wolf, R.K. Campen, Hydrophobic water probed experimentally at the gold electrode/aqueous interface, Angew. Chem., Int. Ed. 56 (15) (2017) 4211–4214.
[88] J.D. Eaves, J.J. Loparo, C.J. Fecko, S.T. Roberts, A. Tokmakoff, P.L. Geissler, Hydrogen bonds in liquid water are broken only fleetingly, Proc. Natl. Acad. Sci. USA 102 (37) (2005) 13019–13022.
[89] S. Nihonyanagi, S. Ye, K. Uosaki, L. Dreesen, C. Humbert, P. Thiry, A. Peremans, Potential-dependent structure of the interfacial water on the gold electrode, Surf. Sci. 573 (1) (2004) 11–16.
[90] D.T. Limmer, A.P. Willard, Nanoscale heterogeneity at the aqueous electrolyte–electrode interface, Chem. Phys. Lett. 620 (2015) 144–150.
[91] S. Zou, Y. Chen, B. Mao, B. Ren, Z. Tian, SERS studies on electrode/electrolyte interfacial water I. Ion effects in the negative potential region, J. Electroanal. Chem. 424 (1–2) (1997) 19–24.
[92] O. Ayemoba, A. Cuesta, Spectroscopic evidence of size-dependent buffering of interfacial pH by cation hydrolysis during CO2 electroreduction, ACS Appl. Mater. Interfaces 9 (33) (2017) 27377–27382, PMID: 28796478.
[93] F. Zhang, A.C. Co, Direct evidence of local pH change and the role of alkali cation during CO2 electroreduction in aqueous media, Angew. Chem., Int. Ed. 59 (4) (2020) 1674–1681.
[94] M.R. Singh, Y. Kwon, Y. Lum, J.W.I. Ager, A.T. Bell, Hydrolysis of electrolyte cations enhances the electrochemical reduction of CO2 over Ag and Cu, J. Am. Chem. Soc. 138 (39) (2016) 13006–13012, PMID: 27626299.
[95] M.C.O. Monteiro, A. Mirabal, L. Jacobse, K. Doblhoff-Dier, S.C. Barton, M.T.M. Koper, Time-resolved local pH measurements during CO2 reduction using scanning electrochemical microscopy: Buffering and tip effects, JACS Au 1 (11) (2021) 1915–1924.
[96] X. Liu, M.C.O. Monteiro, M.T.M. Koper, Interfacial pH measurements during CO2 reduction on gold using a rotating ring-disk electrode, Phys. Chem. Chem. Phys. 25 (2023) 2897–2906.
[97] J.A. Fournier, W. Carpenter, L. De Marco, A. Tokmakoff, Interplay of ion–water and water–water interactions within the hydration shells of nitrate and carbonate directly probed with 2D IR spectroscopy, J. Am. Chem. Soc. 138 (30) (2016) 9634–9645.